




Easy way to produce iron-doped titania nanoparticles via the solid-state method and investigation their photocatalytic activity

Domenico Rosa^{1,a)} , Francesca D'Agostino¹, Irene Bavasso¹, Maria Paola Bracciale¹, Luca Di Palma¹

¹Department of Chemical Engineering Materials Environment & Udr INSTM, Sapienza-Università di Roma, Via Eudossiana 18, 00184 Rome, Italy

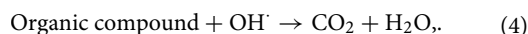
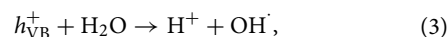
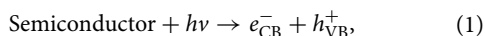
^{a)}Address all correspondence to this author. e-mail: domenico.rosa@uniroma1.it

Received: 24 June 2022; accepted: 23 December 2022; published online: 11 January 2023

This study focuses on the synthesis of iron-doped TiO₂ nanoparticles “via solid-state” method, as an alternative to the more common doping strategies, with different iron content (0.5, 1.0, 1.5, and 2.0 wt%) using commercial titania Degussa P25 and TiO₂ synthesized (sTiO₂) via microemulsion method. The samples were characterized by SEM, BET, UV–Vis-DRS, and XRD. The photocatalytic activity was evaluated in terms of methylene blue (MB) degradation in aqueous solution under visible radiation (LED lamp 13 W) and under different conditions (pH, catalyst dosage, pollutant initial concentration, irradiance). The tests showed a big difference between sTiO₂ and Degussa 25. The sTiO₂ with an iron load of 1.0 wt% (1% Fe–TiO₂) has been proven to be the best photocatalyst. This behavior is attributed to the Fe³⁺ species in sTiO₂ crystal lattice whose presence decreases the bandgap.

Introduction

The current trend in scientific research aims at the synthesis of photocatalytic nanomaterials activated by visible light [1], to be employed in the removal of recalcitrant pollutants (drugs and dyes) from wastewater [2, 3]. The most important photocatalysts are semiconductors which possess a valence band (with full electron) and a conduction band (with higher energy and no electron) with a definite bandgap. The ideal process can be represented in four steps (Eqs. 1–4). The first process involves the adsorption of light of a certain wavelength by a photocatalyst and the formation of electron–hole pair due to the electron excitation from the valence band (VB) to the conduction band (CB) (Eq. 1). The excited electrons can react with electron acceptors such as O₂ on the catalyst surface or dissolved in water and reduce it to form superoxide radical anion O₂^{•−} (Eq. 2). The holes can scavenge H₂O molecules on the surface of the nanoparticle to generate ·OH radicals (Eq. 3) which, due to their high oxidative power (2.8 eV), are able to mineralize organic compounds by producing CO₂ and water (Eq. 4).



The most widely used photocatalyst is titanium dioxide (TiO₂) [4, 5] which is economic [6], non-toxic, available, chemical inert, with high photocatalytic activity [7] as claimed by many authors [8–10]. Schematic photochemical activation of titania is represented in Fig. 1.

However, titania has a bandgap quite high (3.2 eV) and it works only under UV radiation (which is expensive and dangerous for human health). To overcome this problem, it is possible to modify titania using many types of dopants, both non-metals, and metals, but often expensive or hard-to-find reagents are used (for example Er [10], Nd [11]). Doping with iron is cheap and effective to adopt [12, 13] because it reduces the bandgap of titania and easily penetrates the crystal lattice effectively replacing titanium because they have a similar atomic radius. However, even this approach is not without problems because complex and expensive doping strategies are used (hydrothermal magnetization [14], sol–gel method/ultrasound-assisted synthesis [15], plasma-assisted oxidative pyrolysis [16]). Thus, in this work an alternative iron doping strategy has been proposed,

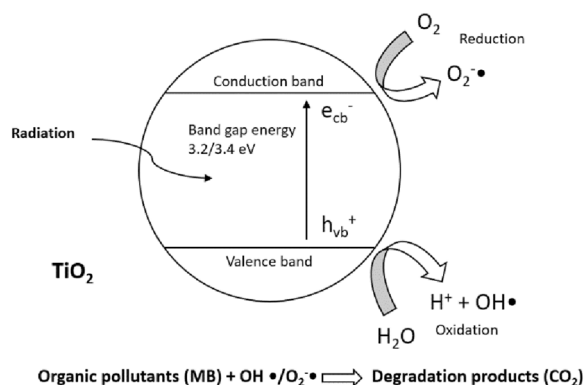


Figure 1: Schematic representation of the photochemical activation of titania and formation of the radical species (hydroxyl and superoxide radicals).

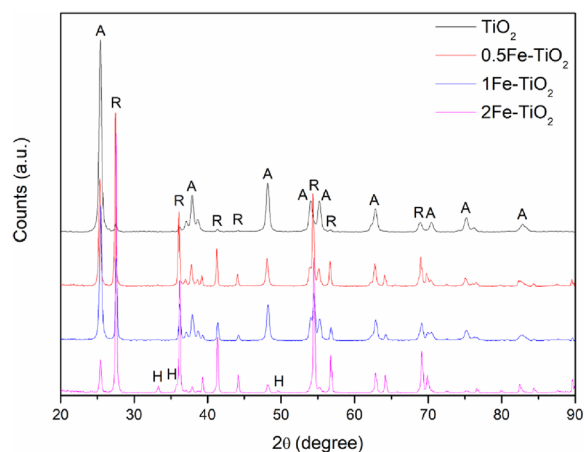


Figure 2: XRD patterns for sTiO₂ and samples with different iron content, (0.5% Fe-TiO₂, 1% Fe-TiO₂ and 2% Fe-TiO₂). A: anatase; R: rutile; H: hematite.

which is easy, effective, and does not produce any residue, the “solid-state” method.

Results and discussion

XRD analysis: crystal phase transformation and identification

The crystalline structure of the sTiO₂-based photocatalysts was determined by XRD analysis, and the patterns are shown in Fig. 2. The pure TiO₂ sample consist mainly of anatase (25.6°) phase and rutile (27.3°) is present only in little amount. The diffraction peaks ascribed to rutile gradually intensifies in Fe-doped samples to the detriment of anatase, which is largely converted at high iron contents (2%). This indicates the doping of Fe can promote the anatase–rutile phase transformations. Indeed, iron species (Fe³⁺) can significantly promote the anatase–rutile transition process [17], causing the generation of relaxation of

apical Ti–O bonds [18]. Furthermore, at the highest iron loading (2%) small amounts of hematite phase (Fe₂O₃) is also detected (33.0°) meaning that not all the Fe³⁺ was able to enter the titania crystal lattice on substitutional sites but it formed a separate phase.

UV-Vis diffuse reflectance spectra

The results of UV-Vis-DRS analysis on Fe-TiO₂ and Fe-P25 are shown in Fig. 3(a, b). The pure TiO₂ has a bandgap of 3.05 eV which is consistent with the bandgap of pure anatase (3.20 eV). The diffuse reflectance spectra of all Fe-TiO₂ samples exhibited a redshift (to the left). The addition of Fe increased absorption in the visible-light range leading to a decrease in the energy bandgap [Fig. 3(b), Table 1] thanks to Ti⁴⁺ substitution by Fe³⁺ in the TiO₂ lattice that forms bands located near the bottom of the conduction band [15].

As the iron content increases (>0.5%), the left side of the bell tends to rise; another phase distinct from TiO₂ is formed, an iron oxide (thus a composite material). In the case of the 2% Fe-TiO₂ sample, the formation of a third phase can be seen due to the presence of a third peak (slightly lower than that of titania), probably another iron oxide.

These results revealed that the iron ions are indeed incorporated into the lattice of TiO₂ because the ionic radius of Ti⁴⁺ (0.68Å) and Fe³⁺ (0.64Å) are almost the same and Fe³⁺ ions can enter the crystal structure of titania [16, 17].

Bandgap energy was estimated from a plot of (αhν)² vs photon energy (hν). The intercept of the tangent to the plot gives a good approximation of the bandgap energy for TiO₂ and the results are reported in Table 1.

For the P25 sample, the doping did not show the same effect and the modification was not as effective as for TiO₂. It is possible to observe a shift of the peak toward lower values with the addition of iron, but without a significant modification in the values that remained almost constant for all three samples (0.5% Fe-P25, 1% Fe-P25, and 2% Fe-P25). With the increase of the iron content, the bell widened, and the left branch tended to rise: Moreover, at increasing iron content, starting from 1%, an iron oxide phase appeared (Fe₂O₃ [12]) and migration into the bulk of titanium dioxide was not observed, there is not peak shift [Fig. 3(a), Table 1].

BET surface areas

The surface area, pore volume and pore size values from the BET analysis were summarized in Table 1 where it could be observed that the decrease of the surface area as the iron content increases for the P25 samples was attributed to pore occlusion while the synthesized TiO₂ had an opposite behavior; in fact, as the iron content increases, the surface area increased probably because of the iron oxides nanoparticles

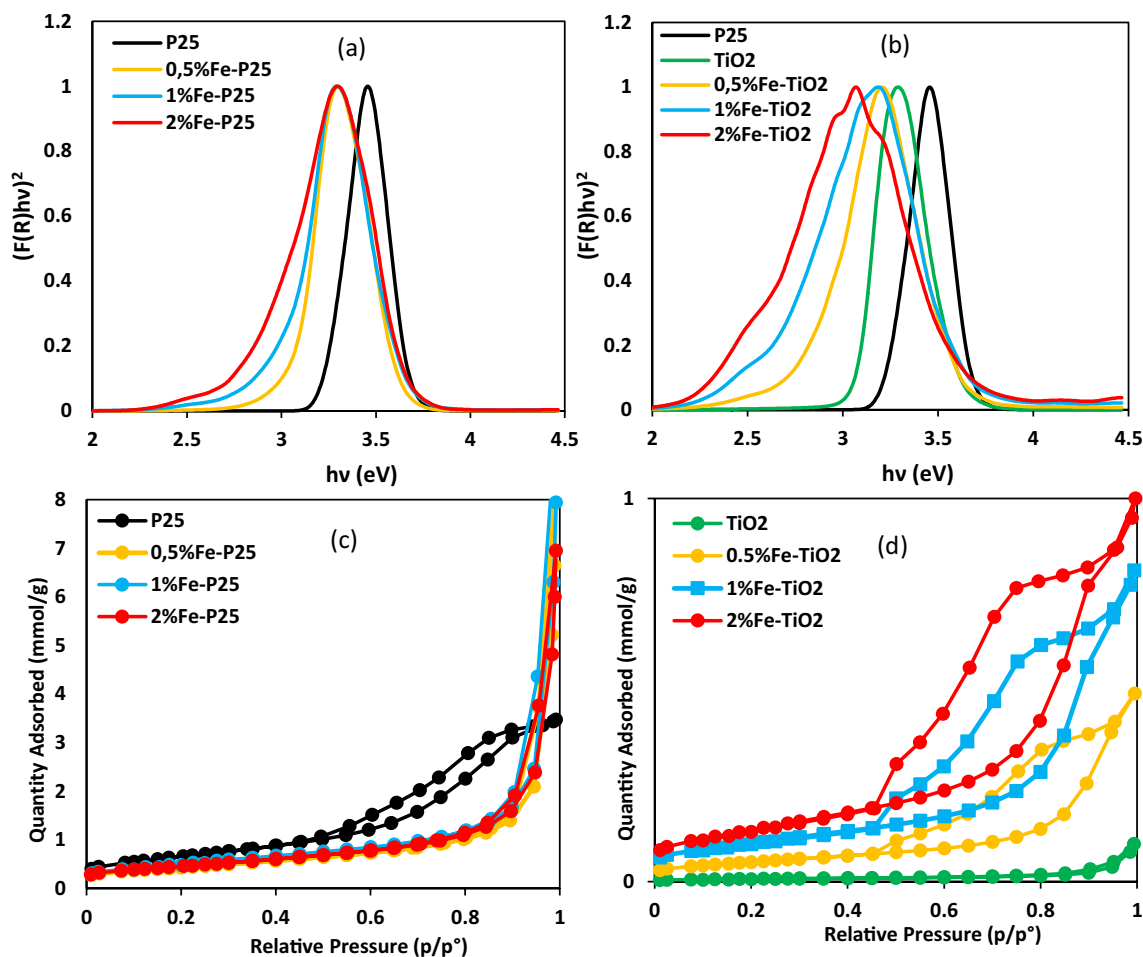


Figure 3: Plot obtained by UV-Vis-DRS analysis for the (a) P25-based and (b) TiO_2 -based nanoparticles doped with different iron content. (c) N_2 adsorption-desorption isotherm for P25 and (d) for synthesized TiO_2 with different iron content.

TABLE 1: The bandgap, surface area, pore volume, and pore size values of samples P25, TiO_2 , and with different iron content.

Sample	Band gap (eV)	BET surface area (m^2/g)	Pore volume (cm^3/g)	Pore size (\AA)
P25	3.20	52.69	0.12	70.83
0.5% Fe-P25	3.05	44.19	0.29	314.40
1% Fe-P25	3.00	40.75	0.32	293.88
2% Fe-P25	2.82	36.07	0.24	254.66
TiO_2	3.05	4.18	0.01	61.50
0.5% Fe- TiO_2	2.81	8.01	0.03	64.24
1% Fe- TiO_2	2.52	9.16	0.03	64.34
2% Fe- TiO_2	2.41	10.86	0.03	50.62

can alleviate thermal sintering of the TiO_2 nanoparticles [13] as supported by SEM investigations showing that Fe- TiO_2 particles are smaller than pure TiO_2 .

Figure 3(c, d) show the N_2 adsorption-desorption isotherms for all samples. It can be observed that pure P25 is a mesoporous material while the addition of iron occludes the pores.

The adsorption isotherm for the sample P25 is a type IV isotherm (according to the IUPAC classification of adsorption isotherms) with a hysteresis cycle; instead, the adsorption isotherms for the samples with iron are type III isotherms, typical of poor interactions between adsorbate and adsorbent material. This result was consistent with that of the UV-Vis-DRS analysis: iron did not migrate into the crystalline bulk of P25 but formed another phase that settles on the surface of the nanoparticle occluding its pores [18].

For the TiO_2 sample, iron into the titania lattice modifies the material. The adsorption isotherm for the pristine TiO_2 is a type III curve, while adsorption isotherms for the samples with iron are type IV curves, characteristic of mesoporous materials [19] [Fig. 3(c, d)].

TiO₂ and Fe–TiO₂ nanoparticles characterization (SEM)

In Fig. 4 SEM images of the titania nanoparticles are reported. The synthesized nanoparticles appear spherical with an average size of 62.76 nm ± 16.74 nm [Fig. 4(a)] and with a homogeneous distribution. The addition of a certain amount of Fe (0.5 wt%) did not produce a morphological modification [12] but had a suppressive effect on the growth of TiO₂ crystals (39.88 nm ± 5.51 nm) since the additives hindered the contact between TiO₂ particles and inhibited crystal growth during heat treatment [15] [Fig. 4(b)].

With the increase of the Fe content, a loss of the spherical form was detected, and the nanoparticles appeared more agglomerated [Fig. 4(c, d)].

Photocatalytic degradation of MB

All the process parameters were tested one by one to find the optimum condition for our system and analysis conducted with

IC on the flow of liquid in contact with the sample (1% Fe–TiO₂) after calcination showed a residual chlorine concentration like the amount present in the deionized water used in the present work (0.33 mg/L) because chloride was completely removed in thermal treatment.

Iron content

Preliminary experimental tests under visible radiation revealed that the adoption of a Fe content in the range (0.5–1.5 wt%) produced an increase in photocatalytic efficiency [Fig. 5(a)] as suggested by the enhancement on MB removal from 35% of pure TiO₂ up to 57% (Fe amount of about 0.5 wt%, 1.0 wt%, and 1.5 wt%). This is because the dopant metal replaces TiO⁴⁺ in the crystalline bulk of TiO₂ bringing improvements in the photocatalytic activity of titania. Fe³⁺ metal cations can act as photogenerated positive hole-electron pairs [20] having the characteristic of both charge donors and acceptors (Fe^{2+/3+}).

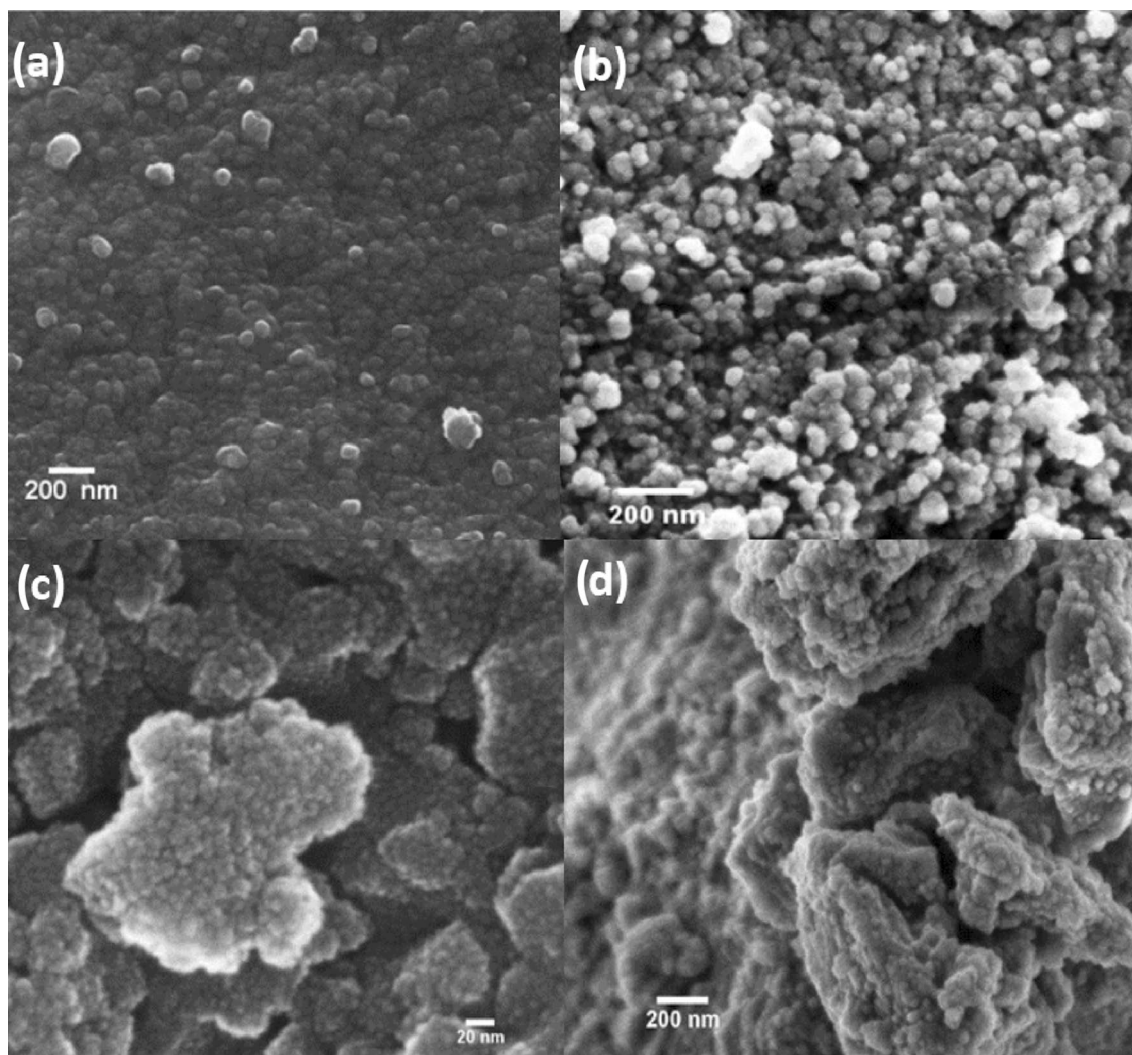


Figure 4: SEM micrographs for the samples (a) TiO₂, (b) 0.5%Fe-TiO₂, (c) 1% Fe-TiO₂, (d) 2% Fe-TiO₂.

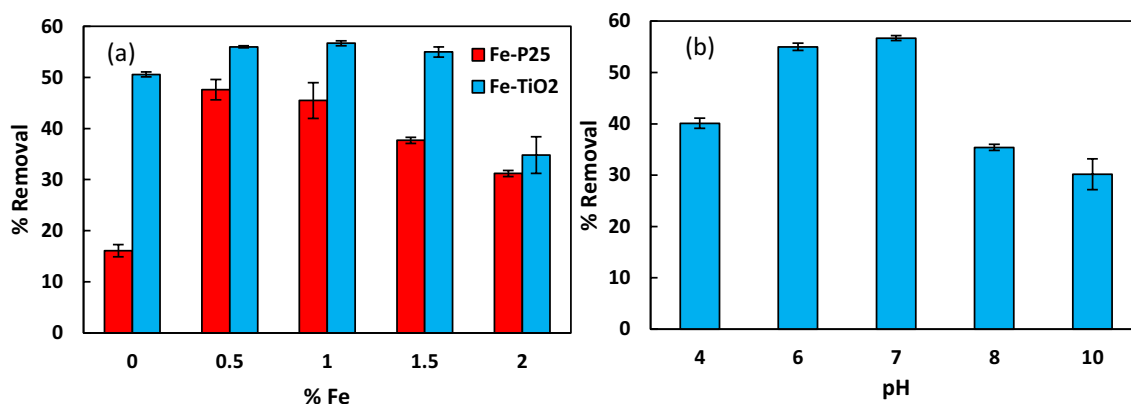


Figure 5: Conditions: Solid: Liquid Ratio (g/L) 1:1, MB initial concentration 5 ppm, time 3 h, and Irradiance 9.4 W/m². (a) Effect of catalyst type on MB removal % pH 7. (b) Effect of pH on MB removal % with 1% Fe-TiO₂.

All these cations were used in low concentrations (typically between 0.5 and 3.0% in moles) because if the doped metal ions concentration increases too much, the photocatalytic activity will decrease since the dopant could act as a recombination site [3] and in addition, the formation of the second phase could be observed (for Fe₂O₃ it occurred at a charge above 2.0% [12]).

Employing the synthesis method proposed in paragraph 4.2 a Fe loading of 1.0 wt% allowed a suitable dispersion of iron species.

A further increase in Fe content (1.5%) did not produce an improvement in MB removal and this can be attributable to the reduction of Ti content in the resulted catalyst and to the effect of Fe³⁺ ions which can act as charge recombination centers, that hinder the formation of radical species and subsequent oxidation of pollutant molecules [13, 15, 16, 18].

Removal tests also showed that TiO₂ achieved higher removal than P25. This result can be attributed to the presence of more structural defects in the TiO₂ synthesized than P25 (hydrogen inclusion, anion vacancies, reduced Ti species, atom displacements from pure phase positions, etc.) as already observed in another study [9].

As a result of these preliminary tests, subsequent tests were performed with 1% Fe-TiO₂.

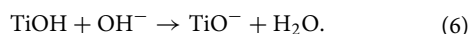
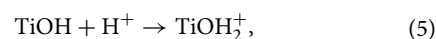
pH

To optimize the operative conditions during the photocatalytic tests, the effect of MB solution pH was analyzed in the range from 4 to 10 and the results are shown in Fig. 5(b).

Results showed that photocatalytic degradation was strongly affected by pH [Fig. 5(b)]. pH in fact is the controlling parameter of the adsorption process (critical step for an efficient photocatalytic degradation) of the organic compound onto the photocatalyst surface, and hence, the degradation reactions rely on the ionization state and also on the surface charge of the photocatalyst and the pollutant

compound [21]. In fact, the radical Hydroxyl, major responsible for pollutant degradation, has a very short lifetime, approx 70 ns, which it means can diffuse (from Einstein-Smoluchowsky equation $\Delta X = \sqrt{2Dt}$, where diffusivity D is $2.3 \times 10^{-5} \text{ cm}^2\text{s}^{-1}$ for $\cdot\text{OH}$ radicals) through an average distance 180 Å [22], which can only degrade the contaminant adsorbed on or near the catalyst surface.

The optimal pH condition was found to be near a neutral (pH 7), pH value at which the catalyst surface is found to be neutral (the pH of zero-charge was estimated to be 7.1 ± 0.3): lower and higher values than 7 produced a detrimental effect on MB removal because at acidic pH conditions catalyst surface could be surrounded by positive charges of H⁺ (Eq. 5) and, therefore, repels cationic MB molecules, inhibiting them from reaching active sites of TiO₂. Under alkaline conditions (pH > 7) the cationic MB molecules might be covered by negative charges, which repel the negatively charged catalyst surface (Eq. 6) [20].



Pollutant concentration

As regards the MB initial concentration, as expected, an increase in MB concentration produced a slight decrease in MB removal from 5 to 15 ppm [Fig. 6(a)] thus suggesting a limiting effect on radicals availability and a delay in MB degradation. At the higher concentration (30 ppm) the degradation was significantly penalized and this because freer radicals and oxidant species for degradation are required and the dark color of the solution affects light penetration [20, 23]. In addition, a large amount of dye is adsorbed on TiO₂ particles which are prevented from dye molecule reaction with free radical and electron-holes [19]. At 50 ppm of MB concentration, no degradation was measured because of the prevention of photocatalytic reaction due to no light penetration.

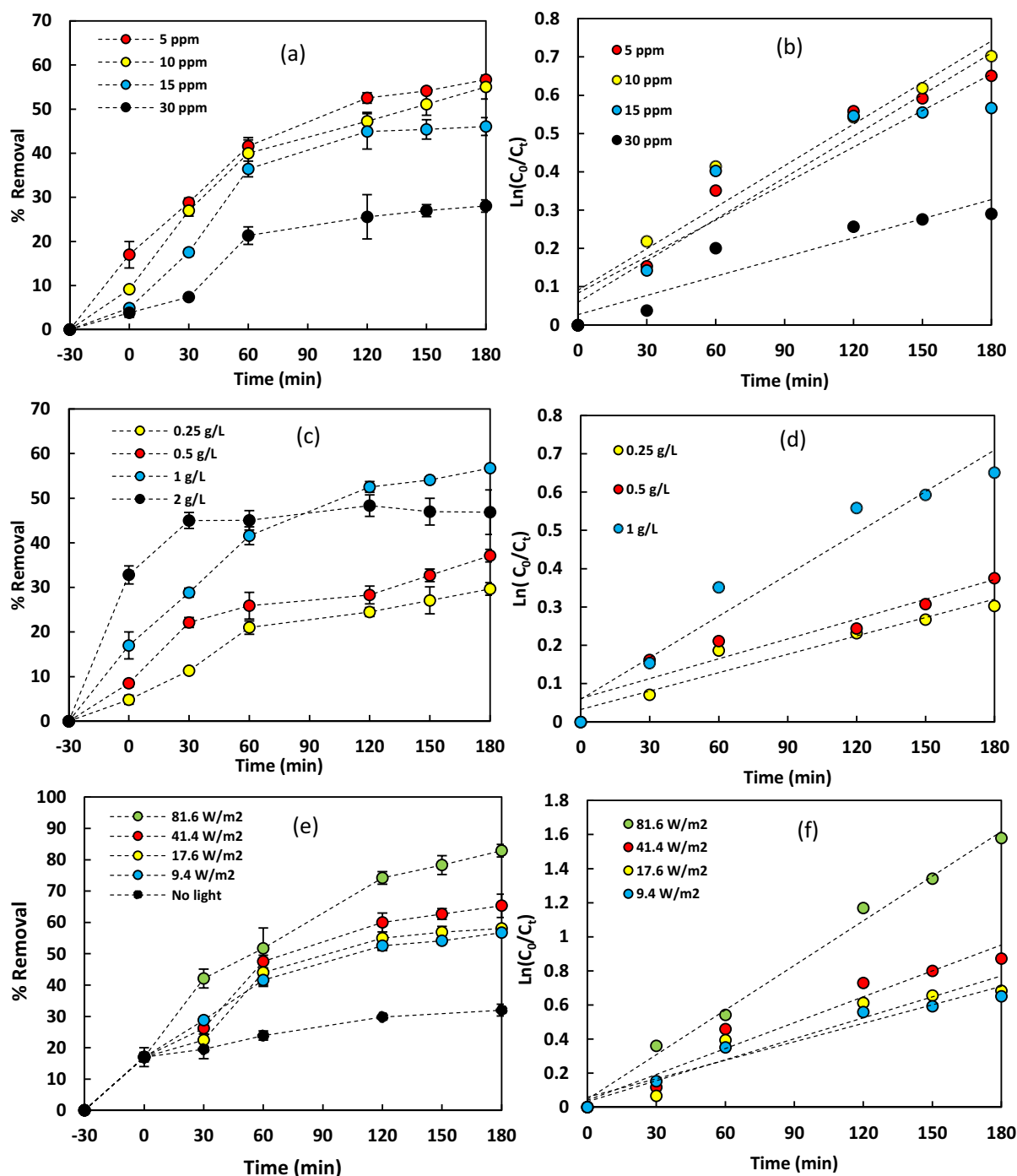


Figure 6: (a) % Removal of MB and (b) first-order kinetic mechanism at different MB concentrations with catalyst dosage 1.00 g/L. (c) % Removal of MB and (d) first-order kinetic mechanism at different catalyst dosages at initial MB concentration 5 ppm. Conditions: pH 7, Irradiance 9.4 W/m² with 1% Fe-TiO₂. (e) % Removal of MB and (f) first-order kinetic mechanism at different irradiance values. Conditions: catalyst dosage 1.00 g/L, pH 7, MB concentration 5 ppm with 1% Fe-TiO₂.

Catalyst dosage

The MB removal increased with the increase of catalyst dosage in the first hour of tests. After that, a plateau on MB removal (45% after 30 min and 47% after 180 min) with a catalyst loading

of about 2.00 g/L was recorded while, in the other tests, the MB removal was ensured in the entire investigated time [Fig. 6(c)] and the optimum was reached by using 1.00 g/L as catalyst loading. The increase in the catalyst dosage contributes to the high

activity because of the presence of more active catalyst sites at higher concentrations, which contribute to the formation of more hydroxide radicals [14, 23]. The presence of a high dosage of a catalyst than 1.00 g/L (above the optimum value) turned the solution to turbid, and this block, scatter and inhibits light penetration for the reaction to proceed, therefore percentage degradation of the MB decreases [1, 19, 20, 23]. The increase in MB removal at 2.00 g/L in the first 60 min can be attributable to the only adsorption mechanism and, even in the case of light activation, the recorded removal was the result of the achievement of equilibrium conditions [1]. To support this evidence, a 1 h of test in dark was conducted and the same MB removal was calculated (about 43%).

A further demonstration of such behavior is provided by R^2 values (close to 1) reported in Table 2, which stands for the correct fitting of linear-type data, typical of the photocatalytic mechanism. Instead doing a linear fitting on the data using 2.00 g/L catalyst yields a value of $R^2 = 0.84$, which means the phenomenon did not follow pseudo-first-order kinetic therefore, the removal of MB cannot be attributed to photocatalysis.

Irradiance

The effect of Irradiance is reported in Fig. 6(e) and as expected, the increase in the light irradiance promoted the MB removal, and at the highest irradiance value adopted the maximum MB removal was calculated (80% in 3 h). The role of photocatalytic activity on the removal of contaminant compared to adsorption alone was evident (tests performed in the absence of light, in 3 h there is 30% removal).

As the irradiance increases, the photon flux incident on the catalyst surface increases, thus increasing the frequency of positive hole-electron pair formation allowing for greater production of hydroxide radicals available for contaminant degradation [24] as described in Fig. 1.

TABLE 2: Kinetic constant and R^2 values for the photocatalytic degradation of MB at different MB concentrations.

MB concentration (ppm)	Catalyst loading (g/L)	Irradiance (W/m ²)	k (min ⁻¹)	R^2
5	1	9.4	0.0036	0.9503
10	1	9.4	0.0036	0.9371
15	1	9.4	0.0032	0.8659
30	1	9.4	0.0017	0.8757
5	0.25	9.4	0.0016	0.9292
5	0.50	9.4	0.0017	0.8927
5	1	81.6	0.0087	0.9933
5	1	41.4	0.0051	0.9510
5	1	17.6	0.0041	0.9190

Occurrence of radical mechanism

To investigate the role of the main active radical species responsible for the degradation of contaminant, the photocatalytic test at 1.00 g/L as catalyst loading and 9.4 W/m² was repeated by adding 0.015 mL of a solution of 20.7 mM of tert-butyl alcohol as ·OH scavenger. The results are reported in Fig. 7 were evident the effect of TBA:

The removal of MB decreased drastically (from 57 to 20% in 3 h) with the addition of the scavenger.

This result confirmed the crucial role of the hydroxyl radical in dye oxidation [18, 23, 25]. The MB removal in tests with TBA was comparable with the effect of the only adsorption mechanism on the catalyst surface [23, 25] which means other radicals like superoxide (O₂^{-·}) had a marginal role in pollutant degradation [26].

Kinetic studies

Removal kinetics were also studied, and pseudo-first-order kinetics (Eq. 7) was defined as a model that best describes the experimental results collected [Fig. 6(b, d and f)].

$$\ln\left(\frac{c_0}{c_t}\right) = k \times t, \quad (7)$$

where c_t is the contaminant concentration at different times t (in min), c_0 the contaminant concentration at time 0, and k the apparent kinetic constant of reaction expressed in min⁻¹. The results of the apparent kinetic constant, as slope of the linear data fitting where in the plots the time has been reported on the x -axis and $\ln\left(\frac{C_0}{C_t}\right)$ on the y -axis., are summarized in Table 2 and are in line with many studies from the literature [12, 19, 20, 23, 27].

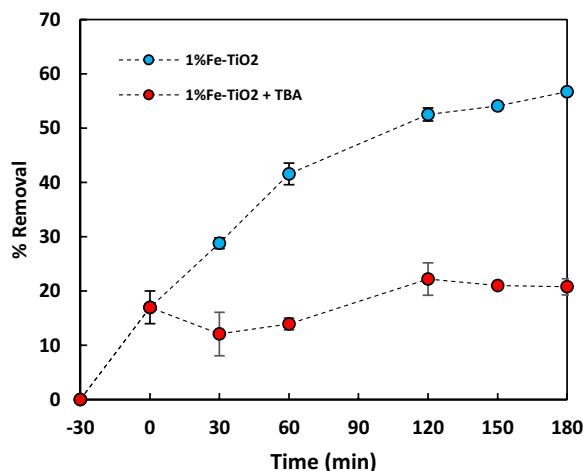


Figure 7: Effect of the addition of TBA on the photocatalytic oxidation of MB. Conditions: 1.00 g/L catalyst, MB concentration 5 ppm, pH 7, and irradiance of 9.4 W/m² with 1% Fe-TiO₂.

The apparent kinetic constant revealed that the parameter that strongly influences the process is irradiation intensity. Although the values of the k are lower than those reported in other works [21, 22], this effect is attributable to the low energy of the source used (13 W respect to 150 [28] 210 [29] or 500 W [26] usually adopted in similar works).

Conclusion

In this work, Fe-doped TiO₂ nanostructures were synthesized via a zero-waste "solid-state" method to be used as photocatalysts in visible light and performing better than commercial titania P25 in the degradation of MB employed as a model contaminant. The 1% Fe-TiO₂ sample proved to be the best performing. The effect of various parameters such as pollutant concentration, catalyst dosage, pH, and irradiation on MB degradation was studied. Better degradation efficiency was obtained using a pH 7 and catalyst dosage of 1.00 g/L. In addition, the degradation efficiency increased as pollutant concentration decreased, and irradiance increased. Irradiance was the parameter that most influenced the process.

To conclude, this research showed how it was possible to synthesize a photocatalytically active material under visible light with an effective, simple, inexpensive method of synthesis using a zero-waste titania doping method, the parameters that most affect the performance of the material were also clarified and explored.

Materials and methods

Chemicals

Titanium diisopropoxide bis-acetylacetonate (75% in isopropanol, Alfa Aesar), Titanium dioxide Degussa P25 (TiO₂ > 99.5% Sigma Aldrich, P25) with purity of 99.9% and particle size < 41 nm, ethanol (absolute, > 99.8%, Honeywell), hexahydrated ferric chloride (FeCl₃ × 6H₂O, Honeywell > 99%), Methylene Blue (MB, C₁₆H₁₈N₃SCl × 3H₂O, Sigma Aldrich), and 20 mM Tert-butyl alcohol solution (> 99.5% Honeywell). All the chemicals were used without any further purification. Deionized water was used as a solvent for preparing all necessary solutions.

Photocatalysts preparation

7.12 mL of Titanium diisopropoxide bis-acetylacetonate (75% in isopropanol) and 20 mL of ethanol were mixed to form a homogenous solution and then the solution was added dropwise to 40 mL of deionized water and stirred for 4 h at 80 °C. After that, the solid was washed several times with deionized water and then dried overnight in an oven at 60 °C. Finally, the solid was ground and calcined at 500 °C for 2 h.

Then, TiO₂ nanoparticles were modified via "solid-state" method. sTiO₂ or P25 and a certain amount of FeCl₃ × 6H₂O

(0.5, 1.0, 1.5, and 2.0 wt% of iron content) were mixed by grinding in a mortar. Then the mixture was calcined in a muffle furnace for 3 h at 600 °C (Fig. 8).

Characterization

The aqueous solution (40 mL) in which the 1%Fe-TiO₂ sample (1 g) was immersed for 2 days was analyzed by ion chromatograph (IC, Thermo Fisher Scientific) to check residual chlorine release after calcification.

The crystalline phases and sizes were determined by X-ray diffraction (XRD) using a Philips Analytical PW1830 X-ray diffractometer, equipped with a Cu K α (1.54056 Å) radiation, in the 2θ range from 5° to 90° with a step size of 0.02° and a time for step of 2 s. The data were collected with an acceleration voltage and applied current of 40 kV and 30 mA, respectively. The crystalline phases in the resulting diffractograms were identified through the COD database (Crystallography Open Database— an open access collection of crystal structures [30]).

The semiconductors' bandgap energy (E_g) can be evaluated from the diffuse reflectance (UV-Vis-DRS) spectrum. Diffuse reflectance UV-Vis spectra (UV-Vis-DRS) to determine the bandgap of the photocatalysts were carried out on a dry pressed disk sample using a spectrophotometer (AvaSpec-2048, Avantes) equipped with a halogen lamp with a tungsten filament (HL-2000 FHSA, Avantes) as a light source. The spectrometer is composed of a diffraction grating of 300 lines/mm, blazed at 500 nm, and a CCD linear sensor (2048 pixels). The reflectance measurements were collected with a spectral resolution of 0.8 nm between 300 and 1100 nm with an integration time of 40 ms and 100 scans. The samples were illuminated at 45° with a bifurcated fiber (diameter of 600 μ m), connected to the halogen lamp, and the reflected light was collected with a 200 μ m diameter fiber at 90° with respect to the surface (45°/0° geometry). A Spectralon standard (Labshere SRS-99-010, 99% reflectance) was taken as a reference for the reflectance spectra.

The optical gap value (E_g) of semiconductors (Table 1) is estimated relying on the Kubelka-Munk method combined with the Tauc relation by the intercepts at $\alpha = 0$ of the linear portion of the $(\alpha h\nu)^2$ versus $h\nu$ of plots.

BET-surface area was calculated from the BET plot determined by N₂ adsorption-desorption isotherms acquired at -196 °C using a Micromeritics Triflex analyzer (Micromeritics Instrument Corp.). The adsorption-desorption N₂ isotherms were acquired in the p/p^0 range from 0.01 to 0.99. Samples were previously outgassed at 200 °C overnight. The BET and BJH equations were used to determine the specific surface area, pore volume, and average pore diameter, respectively.

The morphology of materials was observed by scanning electron microscopy (SEM). SEM images were recorded with a

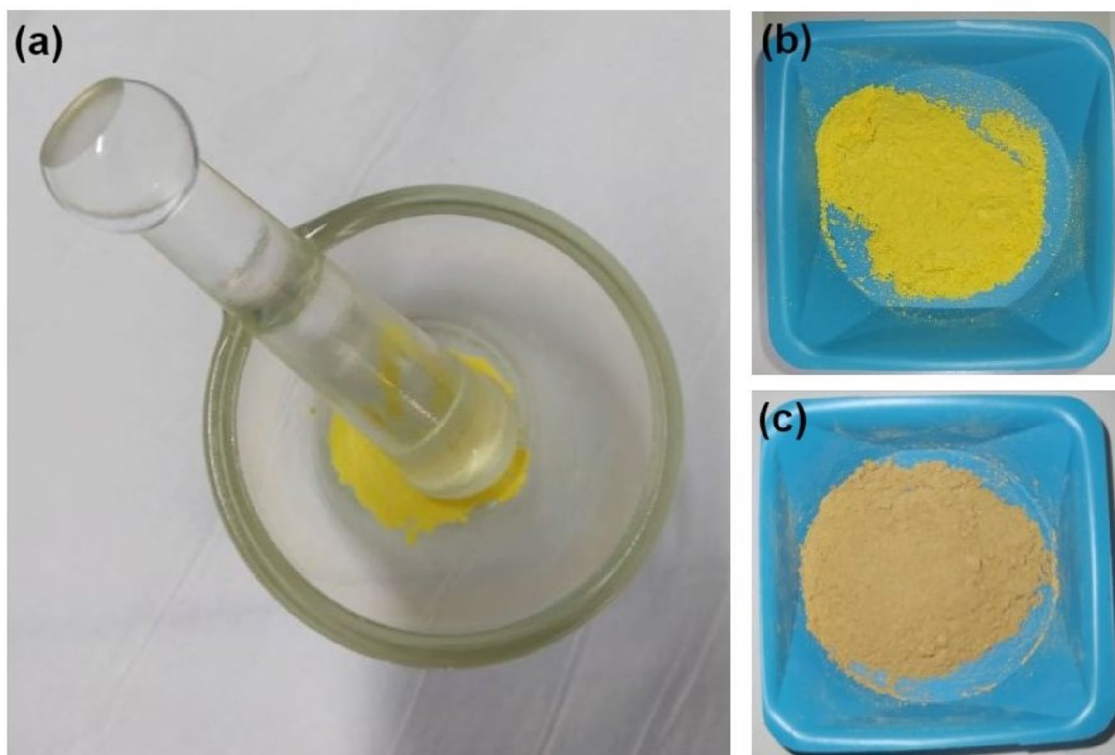


Figure 8: (a) Grinding in the mortar, (b) 1% Fe-TiO₂ before calcination, (c) 1% Fe-TiO₂ after calcination.

High Resolution-Field Emission Scanning Electron Microscope (HR-FESEM, AURIGA Zeiss) operated at 15 kV. The evaluation of nanoparticles' diameter was conducted by using the ImageJ software. All measures, recorded manually, have been elaborated to define an average value and a standard deviation for at least 50 nanoparticles.

Photocatalytic evaluation

The experiments were performed in glass bechers filled with 20 mL of methylene blue (MB) aqueous solution (5 ppm, 10 ppm, 15 ppm, 30 ppm) and different amounts of photocatalyst (0.25 g/L, 0.50 g/L, 1.00 g/L, 2.00 g/L). Moreover, the effect of pH (4, 6, 7, 8, 10) and irradiance (9.4 W/m², 17.6 W/m², 41.4 W/m², 81.6 W/m²) were investigated. The photocatalyst suspensions were stirred during the experiments with a mechanical stirrer at a constant rate of 400 rpm. The light source adopted was a 13 W LED visible-lamp Osram. Before measurements, the aqueous suspension was maintained in the dark for 30 min to attain adsorption-desorption MB equilibrium.

During the photocatalytic tests, MB concentration was determined by UV-vis spectrometry (PG Instruments T80 + UV/Vis spectrophotometer) analysis by measuring the

absorbance at 664 nm. At a specific time (30 min, 60 min, 120 min, 150 min, 180 min), prior to separation of the catalyst from the solution.

In the result analysis, the removal rate of MB was calculated as following:

$$\eta = \frac{A_0 - A(t)}{A_0} \times 100, \quad (8)$$

where η is the MB removal efficiency, A_0 is the MB absorbance after the adsorption/desorption equilibrium was achieved, and $A(t)$ is the MB absorbance of the solution at a specific time t .

Tert-butyl alcohol was used as a scavenger to confirm the occurrence of the radical ·OH.

Acknowledgments

Not applicable.

Author contributions

Conceived and planned the experiments DR, carried out the experiments DR and FD, contributed to the interpretation of the results IB and MPB, wrote the Manuscript DR, supervisor LDP and IB.

Funding

Open access funding provided by Università degli Studi di Roma La Sapienza within the CRUI-CARE Agreement. Not applicable.

Data availability

The datasets used and/or analyzed during the current study are available from the corresponding author on reasonable request.

Declarations

Conflict of interest The authors declare that they have no competing interests.

Ethical approval

Not applicable.

Consent for publication

Not applicable.

Open Access

This article is licensed under a Creative Commons Attribution 4.0 International License, which permits use, sharing, adaptation, distribution and reproduction in any medium or format, as long as you give appropriate credit to the original author(s) and the source, provide a link to the Creative Commons licence, and indicate if changes were made. The images or other third party material in this article are included in the article's Creative Commons licence, unless indicated otherwise in a credit line to the material. If material is not included in the article's Creative Commons licence and your intended use is not permitted by statutory regulation or exceeds the permitted use, you will need to obtain permission directly from the copyright holder. To view a copy of this licence, visit <http://creativecommons.org/licenses/by/4.0/>.

References

1. A.G. Akerdi, S.H. Bahrami, Application of heterogeneous nanosemiconductors for photocatalytic advanced oxidation of organic compounds: a review. *J. Environ. Chem. Eng.* (2019). <https://doi.org/10.1016/j.jece.2019.103283>
2. W. Zhao, I.W. Chen, F. Huang, Toward large-scale water treatment using nanomaterials. *Nano Today* **27**, 11–27 (2019). <https://doi.org/10.1016/j.nantod.2019.05.003>
3. M.S. Mohseni-Salehi, E. Taheri-Nassaj, M. Hosseini-Zori, Effect of dopant (Co, Ni) concentration and hydroxyapatite compositing on photocatalytic activity of titania towards dye degradation.

- J. Photochem. Photobiol. A Chem. **356**, 57–70 (2018). <https://doi.org/10.1016/j.jphotochem.2017.12.027>
4. T. Velepini, E. Prabhakaran, K. Pillay, Recent developments in the use of metal oxides for photocatalytic degradation of pharmaceutical pollutants in water—a review. *Mater. Today Chem.* (2021). <https://doi.org/10.1016/j.mtchem.2020.100380>
5. S.Z. Alsheheri, Nanocomposites containing titanium dioxide for environmental remediation. *Des. Monomers Polym.* **24**(1), 22–45 (2021). <https://doi.org/10.1080/15685551.2021.1876322>
6. Y. Ding et al., Nanoporous TiO₂ spheres with tailored textural properties: controllable synthesis, formation mechanism, and photochemical applications. *Prog. Mater. Sci.* (2020). <https://doi.org/10.1016/j.pmatsci.2019.100620>
7. A.B. Lavand, Y.S. Malghe, S.H. Singh, Synthesis, characterization, and investigation of visible light photocatalytic activity of Cd doped TiO₂/CdS core-shell nanocomposite. *Indian J. Mater. Sci.* **2015**, 1–9 (2015). <https://doi.org/10.1155/2015/690568>
8. C.H.A. Tsang et al., Titanium oxide based photocatalytic materials development and their role of in the air pollutants degradation: overview and forecast. *Environ. Int.* **125**, 200–228 (2019). <https://doi.org/10.1016/j.envint.2019.01.015>
9. I. Barba-Nieto, U. Caudillo-Flores, M. Fernández-García, A. Kubacka, Sunlight-operated TiO₂-Based photocatalysts. *Molecules* (2020). <https://doi.org/10.3390/molecules25174008>
10. S. Obregón, A. Kubacka, M. Fernández-García, G. Colón, High-performance Er³⁺-TiO₂ system: dual up-conversion and electronic role of the lanthanide. *J. Catal.* **299**, 298–306 (2013). <https://doi.org/10.1016/j.jcat.2012.12.021>
11. A. Bokare, M. Pai, A.A. Athawale, Surface modified Nd doped TiO₂ nanoparticles as photocatalysts in UV and solar light irradiation. *Sol. Energy* **91**, 111–119 (2013). <https://doi.org/10.1016/j.solener.2013.02.005>
12. Y. Zhang et al., Highly dispersed titania-supported iron oxide catalysts for efficient heterogeneous photo-Fenton oxidation: Influencing factors, synergistic effects and mechanism insight. *J. Colloid Interface Sci.* **587**, 467–478 (2021). <https://doi.org/10.1016/j.jcis.2020.12.008>
13. M.A. Ahmed, E.E. El-Katori, Z.H. Gharni, Photocatalytic degradation of methylene blue dye using Fe₂O₃/TiO₂ nanoparticles prepared by sol-gel method. *J. Alloys Compd.* **553**, 19–29 (2013). <https://doi.org/10.1016/j.jallcom.2012.10.038>
14. R. Djellabi, B. Yang, H.M. Adeel Sharif, J. Zhang, J. Ali, X. Zhao, Sustainable and easy recoverable magnetic TiO₂-Lignocellulosic Biomass@Fe₃O₄ for solar photocatalytic water remediation. *J. Clean Prod.* **233**, 841–847 (2019). <https://doi.org/10.1016/j.jclepro.2019.06.125>
15. H. Moradi, A. Eshaghi, S.R. Hosseini, K. Ghani, Fabrication of Fe-doped TiO₂ nanoparticles and investigation of photocatalytic decolorization of reactive red 198 under visible light irradiation.

- Ultrason. Sonochem. **32**, 314–319 (2016). <https://doi.org/10.1016/j.ultsonch.2016.03.025>
16. X.H. Wang et al., Pyrogenic iron(III)-doped TiO₂ nanopowders synthesized in RF thermal plasma: phase formation, defect structure, band gap, and magnetic properties. *J. Am. Chem. Soc.* **127**(31), 10982–10990 (2005). <https://doi.org/10.1021/ja051240n>
 17. Y. Yang, Y. Yu, J. Wang, W. Zheng, Y. Cao, Doping and transformation mechanisms of Fe³⁺ ions in Fe-doped TiO₂. *CrystEngComm* **19**(7), 1100–1105 (2017). <https://doi.org/10.1039/c6ce02523d>
 18. G.C. Vásquez et al., Influence of Fe and Al doping on the stabilization of the anatase phase in TiO₂ nanoparticles. *J. Mater. Chem. C Mater.* **2**(48), 10377–10385 (2014). <https://doi.org/10.1039/c4tc02099e>
 19. O.F.S. Khasawneh, P. Palaniandy, P. Palaniandy, M. Ahmadipour, H. Mohammadi, M.R. bin Hamdan, Removal of acetaminophen using Fe₂O₃-TiO₂ nanocomposites by photocatalysis under simulated solar irradiation: optimization study. *J. Environ. Chem. Eng.* (2021). <https://doi.org/10.1016/j.jece.2020.104921>
 20. P.A. Ochoa Rodríguez, G.A. Pecchi, S.G. Casuscelli, V.R. Elías, G.A. Eimer, A simple synthesis way to obtain iron-doped TiO₂ nanoparticles as photocatalytic surfaces. *Chem. Phys. Lett.* (2019). <https://doi.org/10.1016/j.cplett.2019.136643>
 21. J. B. Lingzhiiwang, and M. Juyinglei, *Lecture Notes in Chemistry 100 Photocatalysis Fundamentals, Materials and Applications*. <http://www.springer.com/series/632>. Accessed 8 Jun 2022
 22. F. Hashemzadeh, R. Rahimi, A. Ghaffarinejad, F. Hashemzadeh, R. Rahimi, and A. Gaffarinejad, Photocatalytic degradation of methylene blue and rhodamine b dyes by niobium oxide nanoparticles synthesized via hydrothermal method. (2013) <http://www.ijacsr.com/>. Accessed 25 Nov 2021
 23. H. Mohan et al., Enhanced visible light-driven photocatalysis of iron-oxide/titania composite: norfloxacin degradation mechanism and toxicity study. *J. Hazard Mater.* (2021). <https://doi.org/10.1016/j.jhazmat.2021.125330>
 24. Y. Li, S. Sun, M. Ma, Y. Ouyang, W. Yan, Kinetic study and model of the photocatalytic degradation of rhodamine B (RhB) by a TiO₂-coated activated carbon catalyst: Effects of initial RhB content, light intensity and TiO₂ content in the catalyst. *Chem. Eng. J.* **142**(2), 147–155 (2008). <https://doi.org/10.1016/j.cej.2008.01.009>
 25. V. Kumaravel, S. Mathew, J. Bartlett, S.C. Pillai, Photocatalytic hydrogen production using metal doped TiO₂: a review of recent advances. *Appl. Catal. B Environ.* **244**, 1021 (2019)
 26. T. Ali et al., Photocatalytic performance of Fe-doped TiO₂ nanoparticles under visible-light irradiation. *Mater. Res. Express* (2017). <https://doi.org/10.1088/2053-1591/aa576d>
 27. J. Yu, Q. Xiang, M. Zhou, Preparation, characterization and visible-light-driven photocatalytic activity of Fe-doped titania nanorods and first-principles study for electronic structures. *Appl. Catal. B* **90**(3–4), 595–602 (2009). <https://doi.org/10.1016/j.apcatb.2009.04.021>
 28. S. Sood, A. Umar, S.K. Mehta, S.K. Kansal, Highly effective Fe-doped TiO₂ nanoparticles photocatalysts for visible-light driven photocatalytic degradation of toxic organic compounds. *J. Colloid Interface Sci.* **450**, 213–223 (2015). <https://doi.org/10.1016/j.jcis.2015.03.018>
 29. L. Chen, C. Zhang, L. Wu, K. Lv, K. Deng, T. Wu, A facile one-pot synthesis of biomimetic photocatalyst Zn(II)-porphyrin-sensitized 3D TiO₂ hollow nanoboxes and synergistically enhanced visible-light degradation. *Nanoscale Res. Lett.* (2018). <https://doi.org/10.1186/s11671-018-2745-5>
 30. S. Graulis et al., Crystallography open database—an open-access collection of crystal structures. *J. Appl. Crystallogr.* **42**(4), 726–729 (2009). <https://doi.org/10.1107/S0021889809016690>

Publisher's Note Springer Nature remains neutral with regard to jurisdictional claims in published maps and institutional affiliations.